

Efficient numerical room acoustic simulations with parametrized boundaries using the spectral element and reduced basis method

Hermes Sampedro Llopis^{a,b}, Allan P. Engsig-Karup^c, Cheol-Ho Jeong^a, Finnur Pind^d, Jan S. Hesthaven^e

^a*Acoustic Technology, Department of Electrical Engineering, Technical University of Denmark, Kongens Lyngby, 2800, Denmark*

^b*Rambøll, Hannemanns Allé 53, 2300 København S, Denmark*

^c*Department of Applied Mathematics and Computer Science, Technical University of Denmark, 2800 Kgs. Lyngby, Denmark*

^d*Acoustics and Tactile Engineering, Department of Industrial Engineering, Mechanical Engineering and Computer Science, University of Iceland*

^e*Chair of Computational Mathematics and Simulation Science, École polytechnique fédérale de Lausanne, Lausanne, Switzerland*

Abstract

Numerical methods can be used to simulate wave propagation in rooms, with applications in virtual reality and building design. Such methods can be highly accurate but computationally expensive when simulating high frequencies and large domains for long simulation times. Moreover, it is common that solutions are sought for multiple input parameter values, e.g., in design processes in room acoustics, where different boundary absorption properties are evaluated iteratively. We present a framework that combines a spectral element method (SEM) and a reduced basis method (RBM) to achieve a computational cost reduction for parameterized room acoustic simulations. The SEM provides low dispersion and dissipation properties due to the high-order discretization and the RBM reduces the computational burden further when parametrizing the boundary properties for both frequency-independent and dependent conditions. The problem is solved in the Laplace domain, which avoids instability issues on the reduced model. We demonstrate that the use of high-order discretization and model order reduction has significant advantages for room acoustics in

Email address: hs11c@elektro.dtu.dk (Hermes Sampedro Llopis)

terms of computational efficiency and accuracy.

Keywords: Room acoustic simulations, model order reduction, reduced basis method, Laplace domain

1. Introduction

Room acoustic simulations are used for various purposes, e.g., building design, music, hearing research, entertainment and virtual reality (VR). Historically, these simulations have mostly been carried out by means of geometrical acoustics (GA) methods [1], such as ray tracing. These methods approximate the sound propagation modeling to ensure a manageable computational cost, but cannot simulate wave nature of sound, such as diffraction and interference at low frequencies. The geometrical approximation is known to cause a considerable degradation of the simulation accuracy in many cases [2]. Another approach is to solve directly the governing equations, i.e., the wave equation in the time domain or the Helmholtz equation in the frequency domain, using numerical discretization methods. Different methods have been applied to the room acoustics problem in the past, e.g., the finite element method (FEM) [3], the spectral element method (SEM) [4], the finite difference method (FDTD) [5], the boundary element method (BEM) [6] and the discontinuous Galerkin finite element method [7]. These methods are, in principle, more accurate than GA, as no approximation on the wave propagation is applied except for numerical errors in the discretization. Moreover, wave phenomena such as diffraction and wave interference are inherently accounted for. The main drawback to such an approach is the high computational cost, especially when considering higher frequencies. This makes it difficult to apply them to scenarios where the full audible spectrum and large room dimensions must be taken into account, e.g., simulating a large hall from 20 Hz to 20 kHz. A remaining key challenge in room acoustic simulations is to accelerate the numerical methods used in large scale applications and in cases where the room acoustics is optimized via iterative evaluations of acoustic treatments. Thus, we aim to develop a computational

framework that provides a considerable reduction in the computational cost while producing accurate simulations, with application in virtual reality and building design. A high-fidelity solver based on a high-order spectral element discretization in the Laplace domain is proposed. Past works showed how high-order SEM has the potential of being cost-efficient [8] and suitable for room acoustics due to the low dispersion and dissipation properties, the high geometric flexibility and the possibility of parallel implementations [4]. Nevertheless, additional acceleration is needed, especially for cases where several simulations have to be carried out for a broad parameter range, e.g., in an iterative design process where different boundary absorption properties need to be simulated or when including moving sources in a VR environment. Thus, the proposed framework includes a reduced order model (ROM) to reduce the computational burden of the simulations further.

Reduced basis methods (RBM) represent an emerging field of numerical techniques for solving parametrized problems efficiently when a large number of simulations with different parameter values are needed [9–17]. RBM have been applied in many different fields, e.g., computational fluid dynamics [18, 19], electromagnetics [20, 21], heat transfer [22] and vibroacoustics [23–25]. However, the method has been applied to the wave equation only in a few studies [26–31]. The RBM consists of the following two stages; a pre-computation offline stage where the parameter space is explored to generate a problem-dependent basis, and an online stage, where for a new given parameter value, a Galerkin projection is used to reduce the dimensionality of the problem by utilizing the generated basis. The generation of the basis can be seen as a data-driven technique that relies on a proper orthogonal decomposition (POD). This offline stage is typically computationally costly as it requires multiple full order model (FOM) solutions, so-called “snapshots”. The reduction of the problem’s dimension of the numerical scheme comes with the truncation of the basis, which may be a source of numerical instability in the reduced model even when the FOM is stable. Moreover, it is also known that for wave problems the Kolmogorov N -width, which gives a measure of the RBM, often exhibits a slow decay [32].

A critical challenge in RBM techniques is the instability issue that may appear in long time numerical simulations if not taken care of in the formulation of the method. Remedies have been proposed to address the instability in the time domain [26, 33–35]. However, the problem can be easily addressed by working instead in the frequency domain, which is the main motivation of using the Laplace domain in this work. Previous studies have investigated the use of the Laplace transform for solving the acoustic-elastic wave equation with a FEM, where RBM was used to test different scenarios for structural health monitoring [30]. The combination of ROM and SEM, has been applied and investigated in previous studies, e.g., for the Navier-Stokes equations [36, 37], where a potential synergy between high-orders and reduced basis methods was demonstrated.

When it comes to room acoustics, quick yet accurate evaluations of the room acoustic condition due to changes in the boundary condition are of utmost importance in building design and renovation projects, to ensure timely, knowledge-based decisions throughout the design process. The proposed numerical framework, which combines SEM and RBM, aims to address this issue. The framework has a substantial potential for building designers and acoustic consultants to find an optimum use of acoustic treatment elements, e.g., absorbers and diffusers, to fulfil the acoustic requirement of the building.

The contributions of this paper are as follows: a) it presents and evaluates a high-order numerical framework based on SEM for solving the acoustic wave equation in the Laplace domain in 2D, b) it applies RBM techniques to reduce the high-order full order model in the Laplace domain for both frequency-independent and frequency-dependent boundary conditions and c) it provides a detailed analysis of the benefits and drawbacks of using high-order numerical schemes in combination with RBM techniques and the use of the Laplace domain.

2. Full order model

2.1. Governing equations and discretization

The acoustic wave propagation in a lossless and steady medium is described by the second-order wave equation,

$$\frac{\partial^2 p}{\partial t^2} - c^2 \Delta p = c^2 \frac{\partial q}{\partial t}, \quad \text{in } \Omega \times (0, T], \quad (1)$$

where $p(\mathbf{x}, t)$ is the sound pressure, \mathbf{x} the position in the domain Ω , t is the time in the interval $(0, T]$, c is the speed of sound ($c = 343$ m/s) and q represents a source pressure.

In this study, a Laplace domain approach is considered. The time-dependent problem can be reduced to the computation of the Laplace transform of p evaluated at a fixed complex frequency $s = \sigma + iy$, by multiplying (1) by e^{-st} and integrating in time over the interval $[0, \infty)$ to obtain

$$s^2 \tilde{p} - c^2 \Delta \tilde{p} = c^2 s \tilde{q}, \quad (2)$$

where $\tilde{p}(\mathbf{x}, s)$ is the Laplace transform of $p(\mathbf{x}, t)$. To solve (2) numerically, the spatial derivatives are discretized and each complex frequency is evaluated separately. This provides an advantage in terms of computational effort over a time-domain approach, if $N_s \ll N_t$, where N_s refers to the number of evaluated complex frequencies and N_t to the number of time steps. To provide the discrete form with homogeneous boundary conditions, a finite element approximation space V of globally continuous piecewise polynomials functions of order P is introduced, $V = \{w \in C^0(\Omega); \forall_n \in 1, \dots, K_{el}, w^{(n)} \in \mathbb{P}^P\}$, K_{el} is the number of elements in the domain Ω . In this study, triangular mesh elements are used. By multiplying (2) with a test function w , integrating over the domain and making use of Green's first identity, and, furthermore, neglecting the boundary terms by assuming a rigid boundary case, we obtain

$$\int_{\Omega} s^2 \tilde{p} w d\Omega + c^2 \int_{\Omega} \nabla \tilde{p} \cdot \nabla w d\Omega = \int_{\Omega} c^2 s \tilde{q} w d\Omega. \quad (3)$$

Truncated series expansions for the unknown and source term are introduced

$$\tilde{p}_N = \sum_{j=0}^N \hat{p}(t) \mathcal{N}_j(\mathbf{x}), \quad \tilde{q}_N = \sum_{j=0}^N \hat{q}(t) \mathcal{N}_j(\mathbf{x}), \quad (4)$$

where N is the number of degrees of freedom (DOFs) and $\mathcal{N}_j(\mathbf{x}) \in V$ is a set of global finite element basis function, which have the cardinal property $\mathcal{N}_j(\mathbf{x}_i) = \delta_{ji}$. Substituting (4) in (3), choosing $w = \mathcal{N}_i(\mathbf{x})$ and assuming a two-dimensional domain, where $\mathbf{x} := (x, y)$ and $\nabla = \left(\frac{\partial}{\partial x} + \frac{\partial}{\partial y} \right)$, the following semi-discrete system is obtained

$$(s^2 \mathcal{M} + c^2 (\mathcal{S}_{xx} + \mathcal{S}_{yy})) \mathbf{p} = c^2 s \mathcal{M} \mathbf{q}, \quad (5)$$

where

$$\begin{aligned} \mathcal{M}_{ij} &= \iint_{\Omega} \mathcal{N}_i(x, y) \mathcal{N}_j(x, y) dx dy, \\ (\mathcal{S}_{xx})_{ij} &= \int_{\Omega} \frac{\partial \mathcal{N}_i(x)}{\partial x} \frac{\partial \mathcal{N}_j(x)}{\partial x} dx dy, \\ (\mathcal{S}_{yy})_{ij} &= \int_{\Omega} \frac{\partial \mathcal{N}_i(x, y)}{\partial y} \frac{\partial \mathcal{N}_j(x, y)}{\partial y} dx dy, \\ \mathbf{p} &= [\hat{p}_1, \hat{p}_2, \hat{p}_3, \dots, \hat{p}_N]^T, \\ \mathbf{q} &= [\hat{q}_1, \hat{q}_2, \hat{q}_3, \dots, \hat{q}_N]^T. \end{aligned} \quad (6)$$

Equation (5) can be split into a set of $2N$ real equations for a given frequency $s = \sigma + iy \in \mathcal{C}$, where the solution is written as $\mathbf{p} = \mathbf{p}^\sigma + i\mathbf{p}^y$. This splitting is important for the implementation. After simple manipulations, the system can be written as

$$(\mathbf{K}^\sigma \mathbf{p}^\sigma - \mathbf{K}^y \mathbf{p}^y) + i(\mathbf{K}^y \mathbf{p}^\sigma + \mathbf{K}^\sigma \mathbf{p}^y) = \mathbf{Q}^\sigma + i\mathbf{Q}^y, \quad (7)$$

where

$$\begin{aligned} \mathbf{K}^\sigma &= \mathcal{M} \sigma^2 - \mathcal{M} y^2 + c^2 (\mathcal{S}_{xx} + \mathcal{S}_{yy}), \\ \mathbf{K}^y &= 2\sigma y \mathcal{M}, \\ \mathbf{Q}^\sigma &= c^2 \mathcal{M} (\mathbf{q}^\sigma \sigma - \mathbf{q}^y y), \\ \mathbf{Q}^y &= c^2 \mathcal{M} (\mathbf{q}^\sigma y + \mathbf{q}^y \sigma). \end{aligned} \quad (8)$$

Equation (7) can be written as

$$\begin{bmatrix} \mathbf{K}^\sigma & -\mathbf{K}^y \\ \mathbf{K}^y & \mathbf{K}^\sigma \end{bmatrix} \begin{bmatrix} \mathbf{p}^\sigma \\ \mathbf{p}^y \end{bmatrix} = \begin{bmatrix} \mathbf{Q}^\sigma \\ \mathbf{Q}^y \end{bmatrix} + \begin{bmatrix} \mathcal{P}_0^\sigma \\ \mathcal{P}_0^y \end{bmatrix}. \quad (9)$$

Note that an initial condition is included, defined as

$$\mathcal{P}_0^\sigma = \mathcal{M}(\sigma p_0 + (p_0)_t), \quad \mathcal{P}_0^y = \mathcal{M}(y p_0), \quad (10)$$

where $p_0 = p(\mathbf{x}, 0)$ is the initial condition in the time domain. For this study, a Gaussian pulse is used

$$p_0(x, y) = e^{-\left(\frac{(x-x_0)^2}{\sigma_g^2} + \frac{(y-y_0)^2}{\sigma_g^2}\right)}, \quad (11)$$

where (x_0, y_0) is the position of the source and σ_g is the spatial variance.

2.2. Boundary conditions

2.2.1. Frequency independent boundaries

In room acoustics it is common to define the boundary conditions in terms of the surface impedance Z_s [38]. For harmonic signals, the conservation of momentum yields a proportional relation between the surface normal pressure derivative $\frac{\partial p}{\partial \mathbf{n}}$ and the surface normal velocity at the boundary v_n . Given $Z_s = p/v_n$, the impedance boundary condition is

$$\frac{\partial p}{\partial \mathbf{n}} = -s\rho v_n = -s\rho \frac{p}{Z_s}, \quad (12)$$

where \mathbf{n} is the outward pointing normal vector of the boundary surface Γ and ρ is the density of the medium which in this study is air ($\rho = 1.2 \text{ kg/m}^3$). By Green's first identity, (3) becomes

$$\int_{\Omega} s^2 \tilde{p} w d\Omega + \int_{\Omega} c^2 \nabla \tilde{p} \cdot \nabla w d\Omega - \oint_{\Gamma} c^2 \frac{\partial \tilde{p}}{\partial \mathbf{n}} w d\Gamma = \int_{\Omega} s c^2 \tilde{q} w d\Omega, \quad (13)$$

Substituting (12) into (13) allows elimination of the normal pressure in the boundary integrals

$$\int_{\Omega} s^2 \tilde{p} w d\Omega + \int_{\Omega} c^2 \nabla \tilde{p} \cdot \nabla w d\Omega + \oint_{\Gamma} s c^2 \frac{\rho}{Z_s} \tilde{p} w d\Gamma = \int_{\Omega} s c^2 \tilde{q} w d\Omega. \quad (14)$$

Finally, (5) becomes

$$(s^2 \mathcal{M} + c^2(\mathcal{S}_{xx} + \mathcal{S}_{yy}) + sc^2 \frac{\rho}{Z_s} \mathcal{M}_\Gamma) \mathbf{p} = c^2 s \mathcal{M} \mathbf{q}, \quad (15)$$

where

$$\mathcal{M}_\Gamma = \int_\Gamma \mathcal{N}_i(x, y) \mathcal{N}_j(x, y) d\Gamma. \quad (16)$$

The system in matrix form after splitting into real and imaginary parts has the same general expression as in (9), with

$$\begin{aligned} \mathbf{K}^\sigma &= (\sigma^2 - y^2) \mathcal{M} + c^2(\mathcal{S}_{xx} + \mathcal{S}_{yy}) + \sigma \mathcal{B}, \\ \mathbf{K}^y &= 2\sigma y \mathcal{M} + y \mathcal{B}, \\ \mathbf{Q}^\sigma &= c^2 \mathcal{M}(\mathbf{q}^\sigma \sigma - \mathbf{q}^y y), \\ \mathbf{Q}^y &= c^2 \mathcal{M}(\mathbf{q}^\sigma y + \mathbf{q}^y \sigma), \\ \mathcal{B} &= c^2 \frac{\rho}{Z_s} \mathcal{M}_\Gamma. \end{aligned} \quad (17)$$

2.2.2. Frequency dependent boundaries

The frequency dependent boundary conditions are implemented via the method of auxiliary differential equations (ADE) [4]. The pressure and the particle velocity at the boundaries are related through the following relationship in the Fourier domain

$$V_n(\omega) = \frac{P(\omega)}{Z_s(\omega)} = P(\omega) Y(\omega), \quad (18)$$

where ω is the angular frequency, $Z_s(\omega)$ is the surface impedance at the boundary, $V_n(\omega) = V \cdot \mathbf{n}$ and $Y_s(\omega)$ is the admittance at the boundary, the inverse of Z_s , which can be approximated as a rational function of order Q as follows

$$Y_s(\omega) = \frac{a_0 + \dots + n_Q (-i\omega)^Q}{1 + \dots + b_Q (-i\omega)^Q}, \quad (19)$$

which can be written as

$$Y_s(\omega) = Y_\infty + \sum_{k=1}^L \frac{A_k}{\lambda_k - i\omega} + \sum_{k=1}^S \left(\frac{B_k + iC_k}{a_k + i\beta_k - i\omega} + \frac{B_k - iC_k}{a_k - i\beta_k - i\omega} \right). \quad (20)$$

Hence L is the number of real poles and S is the complex conjugate pole pairs used in the rational function or curve fitting of (19). Applying the inverse Fourier transform and inserting the particle velocity expression, considering that in the time domain it can be written as

$$v_n(t) = \int_{-\infty}^t p(t')y_s(t-t')dt', \quad (21)$$

we recover the final expression given by

$$v(t) = Y_{\infty}p(t) + \sum_{k=1}^P A_k\phi_k(t) + \sum_{k=1}^S 2\left[B_k\psi_k^{(1)}(t) + C_k\psi_k^{(2)}(t)\right], \quad (22)$$

where ϕ_k , $\psi_k^{(1)}$ and $\psi_k^{(2)}$ are the so called accumulators which can be determined by solving the following differential equations

$$\frac{d\phi_k}{dt} + \lambda_k\phi_k(t) = p(t), \quad (23a)$$

$$\frac{d\psi_k^{(1)}}{dt} + \alpha_k\psi_k^{(1)}(t) + \beta\psi_k^{(2)}(t) = p(t), \quad (23b)$$

$$\frac{d\psi_k^{(2)}}{dt} + \alpha_k\psi_k^{(2)}(t) - \beta\psi_k^{(1)}(t) = 0. \quad (23c)$$

The expressions above are transformed into the Laplace domain. The real and imaginary parts of the particle velocity at the boundary become

$$v^{\sigma} = Y_{\infty}p^{\sigma} + \sum_{k=1}^P A_k\phi_k^{\sigma} + \sum_{k=1}^S 2\left[B_k\psi_k^{(1)\sigma}(s) + C_k\psi_k^{(2)\sigma}(s)\right], \quad (24a)$$

$$v^y = Y_{\infty}p^y + \sum_{k=1}^P A_k\phi_k^y + \sum_{k=1}^S 2\left[B_k\psi_k^{(1)y}(s) + C_k\psi_k^{(2)y}(s)\right]. \quad (24b)$$

Moreover, in the Laplace domain (23) are expressed as

$$\phi_k(s) = p(s)(s + \lambda_k)^{-1}, \quad (25a)$$

$$\psi_k^{(2)}(s) = \beta p[(s + \alpha)^2 + \beta^2]^{-1}, \quad (25b)$$

$$\psi_k^{(1)}(s) = (s + \alpha_k)\beta^{-1}\psi_k^{(2)}(s). \quad (25c)$$

The auxiliary differentials equations to be solved can be written in matrix form for the real and imaginary parts

$$\begin{bmatrix} \mathbf{G}^\sigma & -\mathbf{G}^y \\ \mathbf{G}^y & \mathbf{G}^\sigma \end{bmatrix} \begin{bmatrix} \phi^\sigma \\ \phi^y \end{bmatrix} = \begin{bmatrix} p^\sigma \\ p^y \end{bmatrix}, \quad (26)$$

where $\mathbf{G}^\sigma = \sigma + \lambda_k$ and $\mathbf{G}^y = y$. Moreover,

$$\begin{bmatrix} \mathbf{G}^\sigma & -\mathbf{G}^y \\ \mathbf{G}^y & \mathbf{G}^\sigma \end{bmatrix} \begin{bmatrix} \psi^{(2)\sigma} \\ \psi^{(2)y} \end{bmatrix} = \beta \begin{bmatrix} p^\sigma \\ p^y \end{bmatrix}. \quad (27)$$

where $\mathbf{G}^\sigma = \sigma^2 - y^2 + 2\alpha\sigma + \alpha^2 + \beta^2$ and $\mathbf{G}^y = 2\sigma y + 2\alpha y$. Finally, $\psi^{(1)}$ can be obtained by substituting $\psi_k^{(2)}(s)$ into (25c),

$$\psi^{(1)\sigma} = \frac{1}{\beta} \left[(\sigma + \alpha)\psi^{(2)\sigma} - y\psi^{(2)y} \right], \quad (28a)$$

$$\psi^{(1)y} = \frac{1}{\beta} \left[y\psi^{(2)\sigma} + (\sigma + \alpha)\psi^{(2)y} \right]. \quad (28b)$$

Following the same procedure as before the semi-discrete system becomes

$$(s^2\mathcal{M} + c^2(\mathcal{S}_{xx} + \mathcal{S}_{yy}) + sc^2Y_s\mathcal{M}_\Gamma)\mathbf{p} = c^2s\mathcal{M}\mathbf{q}. \quad (29)$$

The procedure to solve the system, including the frequency-dependent boundaries, requires one to first obtain the pressure at the boundaries by from (5). Second, the velocity at the boundaries is calculated by (24a) and (24b). Third, the admittance at the boundaries is calculated as

$$Y_s = Y_s^\sigma + iY_s^y = \frac{\mathbf{v}_{n\Gamma}}{\mathbf{p}_\Gamma} = \frac{\mathbf{v}_{n\Gamma}^\sigma \mathbf{p}_\Gamma^\sigma + \mathbf{v}_{n\Gamma}^y \mathbf{p}_\Gamma^y}{\mathbf{p}_\Gamma^{\sigma^2} + \mathbf{p}_\Gamma^{y^2}} + i \frac{\mathbf{v}_{n\Gamma}^y \mathbf{p}_\Gamma^\sigma - \mathbf{v}_{n\Gamma}^\sigma \mathbf{p}_\Gamma^y}{\mathbf{p}_\Gamma^{\sigma^2} + \mathbf{p}_\Gamma^{y^2}}. \quad (30)$$

Note that $(Y_s^\sigma, Y_s^y) \in \mathbb{R}^{N \times N}$, where N is the number of degrees of freedom. In this study we consider porous materials as frequency dependent boundary conditions. The surface impedance can be estimated using Miki's model [39] in conjunction with a transfer matrix method [40], and mapped to a four pole rational function by using a vector fitting algorithm [41]. Finally, the sound pressure in the domain is solved with (29) which can be written in the general

form given in (9) where

$$\mathbf{K}^\sigma = \mathcal{M}\sigma^2 - \mathcal{M}y^2 + c^2(\mathcal{S}_{xx} + \mathcal{S}_{yy}) + \mathcal{B}^\sigma, \quad (31a)$$

$$\mathbf{K}^y = 2\sigma y\mathcal{M} + \mathcal{B}^y, \quad (31b)$$

$$\mathbf{Q}^\sigma = c^2\mathcal{M}(\mathbf{q}^\sigma\sigma - \mathbf{q}^yy), \quad (31c)$$

$$\mathbf{Q}^y = c^2\mathcal{M}(\mathbf{q}^\sigma y + \mathbf{q}^y\sigma), \quad (31d)$$

$$\mathcal{B}^\sigma = c^2\rho(\sigma Y_s^\sigma - y Y_s^y)\mathcal{M}_{1D}, \quad (31e)$$

$$\mathcal{B}^y = c^2\rho(y Y_s^\sigma + \sigma Y_s^y)\mathcal{M}_{1D}. \quad (31f)$$

2.3. The Laplace domain and time-dependent signal reconstruction

The use of the Laplace domain is mainly motivated to avoid instability issues when reducing the model. Another motivation for using the Laplace domain approach is that it allows for an analysis of the transient response of a system [42], which is beneficial in room acoustics as impulse responses are widely used to characterize a room for a given source and receiver pair. Temporal representations of audio signals are crucial in room acoustic simulations, particularly for playback and auralization purposes. Moreover the impulse response is used for extracting different room acoustic parameters [43]. The time reconstruction can be performed with the inverse Laplace transform given by

$$p(t) = \frac{e^{\sigma t}}{2\pi i} \int_{-\infty}^{\infty} e^{ity} \tilde{p}(\sigma + iy) dy, \quad t > 0, \quad \sigma > \sigma_0, \quad (32)$$

where $\sigma + iy = s$ and σ_0 is the Laplace convergence abscissa. Since (32) is difficult to evaluate analytically, the Weeks method is used here to recover the time-dependent signal [44]. It provides an explicit expression for the time domain signal as an expansion in terms of Laguerre polynomials, at a cost of solving for N_s times the linear system. There are alternative methods to recover the time signal as, i.e., the trapezoidal rule [45] or Talbot's method [46] reviewed in [47]. However Weeks method allows to compute $p(t)$ for any set of t values, whereas the other methods present more limitations. The temporal reconstruction by Weeks method depends on two free parameters (σ, b) , which

can compromise the final results and the efficiency. Weeks method is given by the following approximation

$$p(t) = e^{(\sigma-b)t} \sum_{k=0}^{\infty} a_k L_k(2bt), \quad (33)$$

where $\sigma \in \mathbb{R}$, $b \in \mathbb{R}^+$ are free parameters and L_k is the Laguerre polynomial of degree k . Moreover, a_k are the expansion coefficients which depends on $\tilde{p}(s)$ and are defined as [48]

$$G(\zeta) = \frac{2b}{1-\zeta} \tilde{u}(s) \left(\sigma + b \frac{1+\zeta}{1-\zeta} \right) = \sum_{k=0}^{\infty} a_k \zeta^k, \quad (34)$$

where $\zeta = \frac{iy-b}{iy+b}$. Using Cauchy's formula and changing the variable so that $\zeta = e^{i\theta}$ it follows that

$$a_k = \frac{1}{2\pi i} \int_{|\zeta|=1} \frac{G(\zeta)}{\zeta^{k+1}} d\zeta = \frac{1}{2\pi} \int_{-\pi}^{\pi} G(e^{i\theta}) e^{-ik\theta} d\theta. \quad (35)$$

Applying the midpoint discretization based on $2N_s$ intervals with $\theta_j = j\pi/N_s$ and $\theta_{j+1/2} = (j+1/2)\pi/N_s$, the coefficients a_k for $k = 0, \dots, N_s - 1$ can be approximated as

$$\hat{a}_k = \frac{1}{2N} \sum_{j=-N_s}^{N_s-1} G(e^{i\theta_{j+1/2}}) e^{-ik\theta_{j+1/2}} = \frac{b}{N_s} \sum_{j=-N_s}^{N_s-1} \frac{e^{-ik\theta_{j+1/2}}}{1 - e^{i\theta_{j+1/2}}} \tilde{u} \left(\sigma + b \frac{1 + e^{i\theta_{j+1/2}}}{1 - e^{i\theta_{j+1/2}}} \right). \quad (36)$$

When evaluating $G(\zeta)$ with $\zeta = e^{i\theta_{j+1/2}}$, the frequencies at which $\tilde{p}(s)$ has to be evaluated has a fixed real part and a varying imaginary part

$$s_j = \sigma + ib \frac{\sin(\theta_{j+1/2})}{1 - \cos(\theta_{j+1/2})} = \sigma + ib \frac{\cot(\theta_{j+1/2})}{2}, \quad \text{for } j = -N_s, \dots, N_s - 1. \quad (37)$$

The approximated coefficients can be finally written as

$$\hat{a}_{k,h} = \frac{b}{N_z} \sum_{j=-N_s}^{N_s-1} \frac{e^{-ik\theta_{j+1/2}}}{1 - e^{i\theta_{j+1/2}}} \tilde{p}(s_j), \quad k = 0, \dots, N_z - 1, \quad (38)$$

where $\tilde{p}(s_j)$ is the solution of the system in (9), evaluated for the frequencies $j = -N_s, \dots, N_s - 1$. As (37) is only evaluated for $j = 0, \dots, N_s - 1$, it could be expected that the system has to be extended for $j = -N_s, \dots, N_s - 1$. However, as $\theta_{j+1/2} = -\theta_{2N_s-(j+1/2)}$ for all $j = -N_s, \dots, -1$, it can be shown by

trigonometric identities that in (37), $s_j = s_{(2N_s-j+1)}^*$, where s^* is the complex conjugate of s . As $[\tilde{p}_N^\sigma, \tilde{p}_N^y]^T$ is the solution for $s = s_j$, it is easy to show that $[\tilde{p}_N^\sigma, -\tilde{p}_N^y]^T$ is the solution for $s = s_j^*$. This allows for a reduction in the number of required solutions of the linear system by only computing the solution for $j = -N_s, \dots, -1$. Thus, the expression of $\tilde{p}(s_j)$ in (38) can be substituted by

$$\tilde{p}(s_j) = \tilde{u}_{N,j}^\sigma + i\tilde{u}_{N,j}^y, \quad \text{for } j = 0, \dots, N_s - 1, \quad (39a)$$

$$\tilde{p}(s_k) = \tilde{u}_{N,k}^\sigma - i\tilde{u}_{N,k}^y, \quad \text{for } k = 2N_s - j + 1, \quad j = 0, \dots, N_s - 1 \quad (39b)$$

Finally, the time signal can be expressed as an expansion that can be truncated based on the number of frequencies N_s so that for each point x_i and time t_n

$$p_i(t) = e^{(\sigma-b)t_n} \sum_{k=0}^{N_s-1} \hat{a}_k L_k(2bt_n), \quad \forall i = 1, \dots, N_s, \quad \forall n = 1, \dots, N_t. \quad (40)$$

An appropriate choice of the free parameters is critical for accurate and efficient results. A suboptimal choice may lead to large deviations from the actual solution. Moreover, it may lead to a longer computational time if N_s is not optimal. Note that b is positive and σ has to satisfy $\sigma > \sigma_0$, where σ_0 is the Laplace convergence abscissa, defined as the infimum of all numbers $\text{Re}(s)$ so that (32) is integrable. Larger values of b ensure a fast convergence. On the other hand, for larger time intervals, smaller values are preferable. There are different rules of thumb to find the optimum values for these parameters [49, 50], but as discussed in [30], none of them are convenient for this particular case. Following the approach presented in [30], the parameters are chosen by fixing a given resolution N_s , a number of time steps N_t and computing the solution for different parameter values that are in the end compared with an analytical solution or a high fidelity time solver solution [4]. Hence

$$\sigma^{opt}, b^{opt} = \min_{\sigma, b} \left\| \sum_i (p_i^* - \hat{p}_i^*) \right\|_2^2, \quad (41)$$

where p_i^* is the solution obtained with a time solver and \hat{p}_i^* is the solution obtained by (40). A way to determine the number of complex frequencies N_s is to select the value that provides the same error obtained with the time solver.

Once the parameters are chosen, the N_s truncation of the Laguerre series can be evaluated recursively using, e.g., Clenshaw’s algorithm [51].

3. Reduced order model

The main motivation for reduced basis methods is to obtain a sufficiently accurate solution to a parametrized problem, for any value of the given parameter, at a reduced cost compared to the original high-fidelity solver. The method consists of two stages. First an offline stage, where a set of high-fidelity solutions, called snapshots, are computed for a selected set of parameter values. The evaluation of the FOM for multiple parameter values results in a upfront computational cost and the objective is to capture the relevant dynamic information of the original model. These high-fidelity solutions are used to generate N_{rb} basis functions by using, e.g., POD. The online stage consists of a Galerkin projection where a system of dimension N_{rb} is solved for each new parameter value. Then, the solution is recovered by a linear combination of the pre-generated basis functions. The key challenge of the method is to construct the reduced basis that preserves the physics dynamics for a required accuracy level.

The high-fidelity solutions $\tilde{p}_{fb}(\mathbf{x}, s, \mu) = p^T$ of the parametrized problem under the variation of the parameter μ , belonging to the parameter space \mathbb{P} , defines the solution manifold

$$\mathcal{M}_{fb} = \{\mu \in \mathbb{P} | \tilde{p}_{fb} \subset \mathbb{V}_{fb}\}, \quad (42)$$

where \mathbb{V}_{fb} is the discrete approximation space. The ultimate goal of the method is to approximate any part of the solution manifold with a small number of basis functions $\{\phi_i\}_{i=1}^{N_{rb}}$. Thus, the reduced space can be expressed as $\mathbb{V}_{fb} = \text{span}\{\phi_1, \dots, \phi_{N_{rb}}\}$. The solution of the PDE is expressed as an expansion of the reduced basis functions $\phi_i(x)$ and the coefficients $a_i(s)$ in the Laplace domain,

$$\tilde{p}_{fb}(x, s, \mu) \approx \tilde{p}_{rb}(x, s, \mu) = \sum_{i=1}^{N_{rb}} \phi_i(x) a_i(s, \mu). \quad (43)$$

A standard way to generate basis functions is by using POD. This technique is used for data compression and low-dimensional approximations and provides an orthogonal basis in the least-square sense. The reduced models can be obtained by truncating the basis while keeping the essential information that ensures the desired accuracy of the results. The generation of the basis consists of performing a uniform sampling of the parameter space $\mathbb{P}_h \subset \mathbb{P}$ where each sample is called a snapshot. The snapshots are collected into a snapshot matrix

$$\mathbf{S} = [\tilde{p}_{fb}(x, s_1), \dots, \tilde{p}_{fb}(x, s_{N_s})], \quad (44)$$

where N_s is the number of complex frequencies. After solving (9), the snapshot matrix can be written as

$$\mathbf{S} = \begin{bmatrix} \mathbf{S}^\sigma \\ \mathbf{S}^y \end{bmatrix} \in \mathbb{R}^{2N \times N_s}, \quad (45)$$

where N is the number of DOFs. Note that the basis functions are orthogonal. Thus, they can be generated by solving the singular value decomposition (SVD) to the snapshot matrix \mathbf{S}

$$\mathbf{S} = \mathbf{U}\mathbf{\Sigma}\mathbf{V}^T. \quad (46)$$

Thus, $\mathbf{\Phi} = [U_1, \dots, U_{N_{rb}}] \in \mathbb{C}^{2N \times N_{rb}}$, where U_i corresponds to the i th singular vector. In practice the number of basis functions N_{rb} can be chosen by a prescribed tolerance ϵ_{POD}

$$E/E_0(N_{rb}) = \frac{\sum_{i=1}^{N_{rb}} \delta_i^2}{\sum_{i=1}^N \delta_i^2} \geq 1 - \epsilon_{POD}, \quad (47)$$

where δ_i correspond to the values of the diagonal of the matrix $\mathbf{\Sigma} = \text{diag}(\delta_1, \dots, \delta_{N_s})$.

To preserve the structure of the high-fidelity matrix \mathbf{K} , a symplectic decomposition (PSD) with a symplectic Galerkin projection is used. Specifically, the *cotangent-lift* method introduced in [52], is applied. It ensures a symplectic matrix in block-diagonal form. Thus, the snapshot matrix (45) is now considered in an extended form

$$\mathbf{S}_{cl} = \begin{bmatrix} \mathbf{S}^\sigma \\ \mathbf{S}^y \end{bmatrix} \in \mathbb{R}^{N \times 2N_s}, \quad (48)$$

which can be decomposed in the same way as before by using an SVD to get the corresponding POD basis, defined as $\Phi = [U_1, \dots, U_{N_{rb}}] \in \mathbb{C}^{N \times 2N_{rb}}$. Then, the symplectic basis is constructed as

$$\Phi_{cl} = \begin{bmatrix} \Phi & \mathbf{0} \\ \mathbf{0} & \Phi \end{bmatrix}. \quad (49)$$

The ROM is built with a Galerkin projection. The solution can be represented as an expansion of POD basis functions that embed the spatial dynamics and the coordinate system a_u in the Laplace domain.

The matrix expression for the real and imaginary parts of (43) is

$$\begin{bmatrix} \tilde{p}_{rb}^\sigma \\ \tilde{p}_{rb}^y \end{bmatrix} = \begin{bmatrix} \Phi a^\sigma \\ \Phi a^y \end{bmatrix}. \quad (50)$$

After inserting (50) into (7), the problem is similar to (9) but now consists of solving a_u

$$\mathbf{K}_{rb} \begin{bmatrix} a^\sigma \\ a^y \end{bmatrix} = \mathbf{q}_{rb}, \quad (51)$$

where a^σ and a^y are the real and imaginary part of the solution. Moreover,

$$\mathbf{K}_{rb} = \Phi_{cl}^T \mathbf{K} \Phi_{cl} = \begin{bmatrix} \Phi & 0 \\ 0 & \Phi \end{bmatrix}^T \begin{bmatrix} \mathbf{K}^\sigma & -\mathbf{K}^y \\ \mathbf{K}^y & \mathbf{K}^\sigma \end{bmatrix} \begin{bmatrix} \Phi & 0 \\ 0 & \Phi \end{bmatrix}, \quad \mathbf{q}_{rb} = \Phi_{cl}^T \begin{bmatrix} \hat{\mathbf{Q}}_{Re}^{\mathcal{M}} \\ \hat{\mathbf{Q}}_{Im}^{\mathcal{M}} \end{bmatrix}. \quad (52)$$

For rigid boundary conditions the operator can be written as

$$\mathbf{K}_{rb} = \begin{bmatrix} \Phi \mathbf{K}^\sigma \Phi^T & -\Phi^T \mathbf{K}^y \Phi \\ \Phi \mathbf{K}^y \Phi^T & \Phi^T \mathbf{K}^\sigma \Phi \end{bmatrix} = \begin{bmatrix} \mathbf{K}_\Phi^\sigma & -\mathbf{K}_\Phi^y \\ \mathbf{K}_\Phi^y & \mathbf{K}_\Phi^\sigma \end{bmatrix}, \quad (53)$$

where

$$\mathbf{K}_\Phi^\sigma = (\sigma^2 - y^2) \mathcal{M}_\Phi + c^2 \mathcal{S}_\Phi, \quad \mathcal{M}_\Phi = \Phi^T \mathcal{M} \Phi, \quad (54a)$$

$$\mathbf{K}_\Phi^y = 2\sigma y \mathcal{M}_\Phi, \quad \mathcal{S}_\Phi = \Phi^T (\mathcal{S}_{xx} + \mathcal{S}_{yy}) \Phi. \quad (54b)$$

For the case where the system is excited with an initial condition the expression becomes

$$\mathbf{q}_{rb} = \Phi_{cl}^T \begin{bmatrix} \mathcal{P}_0^\sigma \\ \mathcal{P}_0^y \end{bmatrix} = \begin{bmatrix} \Phi & 0 \\ 0 & \Phi \end{bmatrix}^T \begin{bmatrix} \mathcal{P}_0^\sigma \\ \mathcal{P}_0^y \end{bmatrix} = \begin{bmatrix} (\mathcal{P}_0^\sigma)_\Phi \\ (\mathcal{P}_0^y)_\Phi \end{bmatrix}, \quad (55)$$

where

$$(\mathcal{P}_0^\sigma)_\Phi = \mathcal{M}_{\Phi q}(\sigma u_0 + (u_0)_t), \quad \mathcal{M}_{\Phi q} = \Phi^T \mathcal{M}, \quad (56a)$$

$$(\mathcal{P}_0^y)_\Phi = \mathcal{M}_{\Phi q}(y u_0). \quad (56b)$$

The solution $[\tilde{u}_{rb}^\sigma, \tilde{u}_{rb}^y]^T$ is finally transformed to the time domain by applying Weeks method.

3.1. ROM with boundary conditions

The same procedure is followed when considering impedance boundary conditions. The expression of the operator \mathbf{K}_{rb} in (53) becomes

$$\mathbf{K}_\Phi^\sigma = (\sigma^2 - y^2)\mathcal{M}_\Phi + c^2\mathcal{S}_\Phi + \sigma\mathcal{B}_\Phi^\sigma, \quad (57a)$$

$$\mathbf{K}_\Phi^y = 2\sigma y\mathcal{M}_\Phi + y\mathcal{B}_\Phi^y, \quad (57b)$$

where \mathcal{M}_Φ and \mathcal{S}_Φ are defined in (54a) and (54b) respectively. In this particular case, $\mathcal{B}_\Phi^\sigma = \mathcal{B}_\Phi^y = \Phi^T \mathcal{B} \Phi$, where \mathcal{B} is defined in (17).

The parameter μ corresponds to the surface impedance Z_s . It is sampled to generate the snapshots for every complex frequency so that $\mathbf{S} \in \mathbb{R}^{N \times 2kN_s}$, where k is the number of sampled impedance values.

The frequency dependent boundary conditions are treated in a similar way. First, the real and imaginary parts of the pressure without considering the boundaries are computed at all boundary nodes. These values are used in (24a) and (24b), to compute the real and imaginary components of the normal velocity at the boundary. Making use of (30), the admittance at the boundaries is computed. Finally, (53) can be solved where the operator \mathbf{K}_{rb} has the same

expression as in (57a). Referring to (31f) and (31e), the boundary terms are written as

$$\mathcal{B}_\Phi^\sigma = \Phi^T \mathcal{B}^\sigma \Phi, \quad (58a)$$

$$\mathcal{B}_\Phi^y = \Phi^T \mathcal{B}^y \Phi. \quad (58b)$$

Note that this operation needs to be computed in every frequency step to update the impedance value at the surface. This increases the computational cost, which leads in lower speedups compared to the frequency-independent case.

4. Numerical experiments

This section examines numerical test cases to give insights into the different properties of the FOM and ROM.

4.1. Dispersion analysis

Previous studies have presented the dispersive and dissipative properties of the SEM for different wave propagation problems [53–60]. It is of particular interest to highlight that the SEM is non-dissipative for wave problems [53]. The dispersion properties of the numerical scheme can be analyzed by using a multi-modal analysis [4, 59]. This provides information about the resolution requirements for resolving a wave accurately. The analysis takes into account all the dispersive properties of the scheme. Here, it is based on the 1D advection equation that represents a single mode in the Euler equation

$$\frac{\partial u}{\partial t} + c \frac{\partial u}{\partial x} = 0. \quad (59)$$

The analysis is conducted to highlight the tight connection between FOM and ROM. Analysis is here done using a propagation speed $c = \omega/k = 1$ m/s, $N_s = 500$ and $\Delta t = 1 \times 10^{-4}$ s. The number of elements is adjusted to evaluate the different points per wavelength (PPW). Figure 1 shows the ratio of the numerical and physical propagation speed c_d/c for different PPW , computed for $P = 1, 2, 3, 4$. A 2% error threshold is defined, as there is some evidence indicating that the perceptual auditory threshold for dispersion errors is around 2%

[61]. As expected the higher the P , the smaller the PPW required. Moreover, the results show that the ROM keeps the dispersion properties of the FOM, which is attributed to the typical exponential convergence property of the SVD decomposition towards the FOM representation. This behaviour remains for higher spatial dimensions, e.g., 2D or 3D.

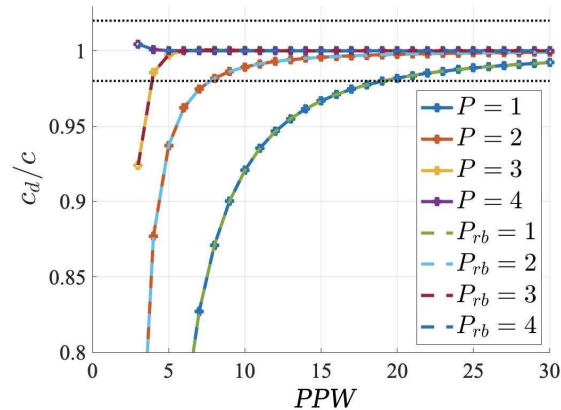


Figure 1: Numerical dispersion relations in 1D using a multi-modal analysis that includes temporal and spatial errors. Analysis computed with $c = 1$ m/s, $N_s = 500$ and $\Delta t = 1 \times 10^{-4}$ s. Full lines correspond to the FOM and dotted lines to the ROM.

4.2. Full Order Model

Full order simulations with frequency-independent boundary conditions and frequency-dependent boundary conditions will be presented.

4.2.1. Square with rigid boundaries

The first test case presented is a 2D domain of size $2 \text{ m} \times 2 \text{ m}$ with rigid boundary conditions, whose analytical solution is known [62]. The simulations were carried out for different polynomial orders ($P = 1, 2, 4, 6$), with a fixed number of elements per dimension $N_{el} = 15$. The respective spatial resolution for the different orders is presented in Table 1. The model was excited with a Gaussian pulse as initial condition (11) with a spatial variance $\sigma_g = 0.2$. The number of complex frequencies can be chosen to match the error obtained with

the time domain solver [4]. In this case it was fixed to $N_s = 6600$ for a simulation time of $t = 0.3$ s. The resulting Weeks parameters obtained with (41) for the presented scenario are $\sigma = 30$ and $b = 1300$. Figure 2 is obtained by applying FFT to the recovered time signal. The error for the different orders is presented in Table 1, defined as $\epsilon_{P_i} = \|p_{an} - p_{SEM}\|_\infty$ for the frequency range of 20 Hz - 1200 Hz. The results show that the use of high-order polynomial functions lead to a lower error, which is a result of the dispersion properties. This error includes both a mismatch of the modal frequencies and their amplitudes.

Table 1: *PPW* and error ϵ_{P_i} for different orders calculated for the frequency range of 20 Hz - 1200 Hz of the results presented in Figure 2.

P	1	2	4	6
PPW (1 kHz)	2.6	5.7	10.4	15.6
ϵ_{P_i} (dB)	22.5	20.1	1.3	0.2

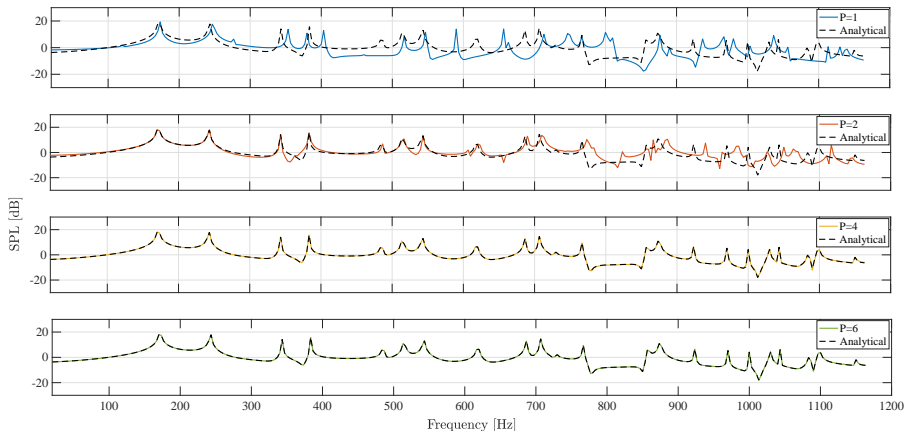


Figure 2: Simulated frequency response of a $2 \text{ m} \times 2 \text{ m}$ square domain with rigid boundaries for basis orders $P = 1, 2, 4, 6$ while using a fixed number of elements per dimension $N_{el} = 15$, $N_s = 6600$, $(\sigma, b) = (30, 1300)$ and $t = 0.3$ s. The source location is $(s_x, s_y) = (1, 1)$ m and the receiver $(r_x, r_y) = (0.2, 0.2)$ m. Analytic solution [62].

The computational time for each frequency step is obtained for different

values of the total number of DOFs N and presented in Figure 3. Note that these values need to be multiplied by the corresponding N_s to obtain the total simulation time. As it is shown, the CPU time increases when increasing N as $\mathcal{O}(N)$.

Finally, the performance of the solver is compared to a time domain solver [4] using the same domain described above with $N_{el} = 15$, $P = 4$ and $\sigma_g = 0.3$, simulated for $t = 0.3$ s. The time step was selected following the global Courant-Friedrichs-Lewy (CFL) condition

$$\Delta t = C_{CFL} \min(\Delta r_i) \min \frac{r_D}{c}, \quad (60)$$

where Δr_i corresponds to the grid spacing between the Legendre-Gauss-Lobatto (LGL) nodes in the 1D reference element and $r_D = A/l_{per}$ is the radius of the triangular elements' inscribed circle. Half of the triangle perimeter is denoted by l_{per} and the area of the triangle by A . In this case, $C_{CFL} = 0.75$ and $\Delta t = 2.95 \times 10^{-5}$ s. The same time step is used for the Weeks method where N_s is selected to provide the same error, comparing against the analytical solution [62], defined as $\epsilon_{SEM} = |p_{an} - p_{SEM}| = 4 \times 10^{-5}$ Pa at the final time step for a receiver position $(r_x, r_y) = (0.2, 0.2)$ m. In this particular case, the number of time steps is $N_t = 10175$ while the number of frequencies is $N_s = 5450$ (with $\sigma = 30$ and $b = 1300$). As it is found that $N_s < N_t$ for the same error, the frequency domain approach can reduce the computational burden. For this particular case, the frequency domain approach is found to be four times faster.

4.2.2. Square with frequency-independent boundaries

In this section a 2D domain with frequency-independent boundary conditions is considered. The simulations are carried out for a 2 m \times 2 m domain. The number of elements per direction is set to $N_{el} = 20$ and a basis order of $P = 4$ is used. The spatial resolution in this case corresponds to roughly 13 *PPW* at 1 kHz. The model is excited with a Gaussian pulse as initial condition (11) with $\sigma_g = 0.2$. First, the model is tested with frequency-independent boundaries with a surface impedance of $Z_s = [500, 15000]$ $\text{kgs}^{-1}\text{m}^{-2}$, which correspond to

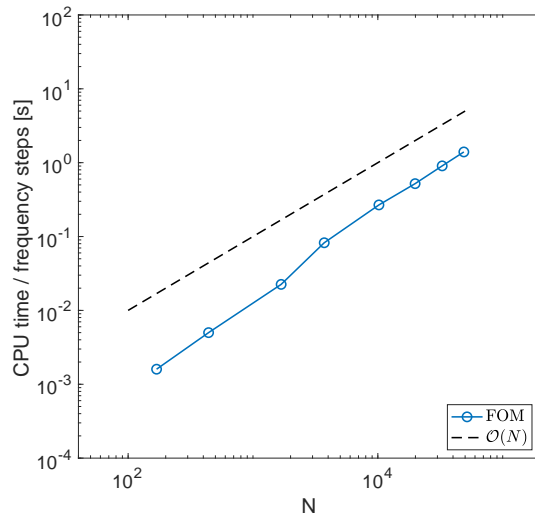


Figure 3: CPU time per frequency step for different degree of freedom N . Computed with $P = 4$, $N_s = 400$, $\sigma = 600$, $b = 950$, $t = 0.01$ s, $\Delta t = 2.95 \times 10^{-5}$ s.

the normal incidence absorption coefficient value $\alpha = [0.99, 0.10]$, calculated using

$$\alpha = 1 - \left| \frac{Z_s - \rho c}{Z_s + \rho c} \right|^2. \quad (61)$$

The time step was selected following the global CFL condition for the time domain solver defined as [4]. The parameters for the Weeks time reconstruction when using $N_s = 3000$ are $\sigma = 10$ and $b = 1000$. The simulated pressure at one receiver point is verified by comparing with a high-fidelity SEM time domain solver [4]. Figure 4 shows good agreement between the two solvers. For the particular case of $Z_s = 15000 \text{ kgs}^{-1}\text{m}^{-2}$, the error at the receiver point at $t = 0.1$ s is $\epsilon = |p_{\text{Time}} - p_{\text{Laplace}}| = 8 \times 10^{-5}$ Pa.

4.2.3. Square with frequency-dependent boundaries

For simplicity, the same domain and parameters from Section 4.2.2 are used except $N_{el} = 15$. The boundary is modelled as a porous material mounted on a rigid backing. The flow resistivity of the material is $\sigma_{mat} = 10000 \text{ Nsm}^{-4}$ and the thickness has values $d_{mat} = [0.05, 0.2]$ m. The surface impedance are

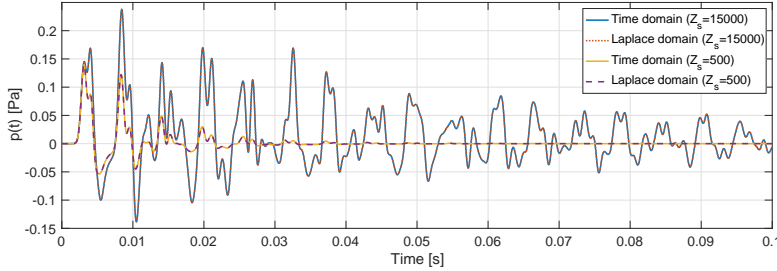


Figure 4: Impulse response simulation with frequency-independent boundaries for different surface impedance values. The source location is $(s_x, s_y) = (1, 1)$ m and the receiver location is $(r_x, r_y) = (0.2, 0.2)$ m. Simulations were carried out with $P = 4$, $\Delta t = 5.9 \times 10^{-6}$ s, $N_{el} = 20$, $N_s = 3000$ and $(\sigma, b) = (10, 1000)$.

estimated using Miki's model [39] in conjunction with a transfer matrix method [40]. The corresponding absorption coefficient according to (61) is presented in Figure 5.

Again the results were verified by comparing with a high-fidelity SEM time domain solver [4]. Figure 6 confirms a good match between the two solvers. For the particular case of $d_{mat} = 0.05$ m, the error was calculated at the receiver point and $t = 0.05$ s, as $\epsilon = |p_{Time} - p_{Laplace}| = 3 \times 10^{-5}$ Pa.

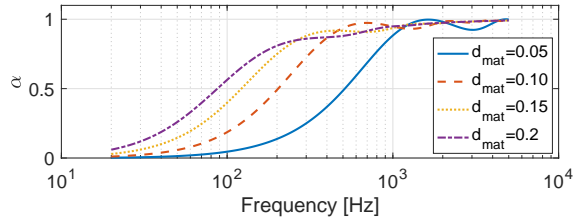


Figure 5: Absorption coefficient for different material thickness d_{mat} (in meters).

4.2.4. Analysis of the influence of the Weeks free parameters

The free parameters of the Weeks method (σ, b) are identified using (41). The error is estimated while using $N_s = 7000$ and 11 equally spaced points for $\sigma \in [0.1, 2000]$ and 11 equally spaced points for $b \in [0.1, 90]$ for rigid boundary conditions and frequency-independent boundaries with $Z_s = 15000 \text{ kgs}^{-1}\text{m}^{-2}$

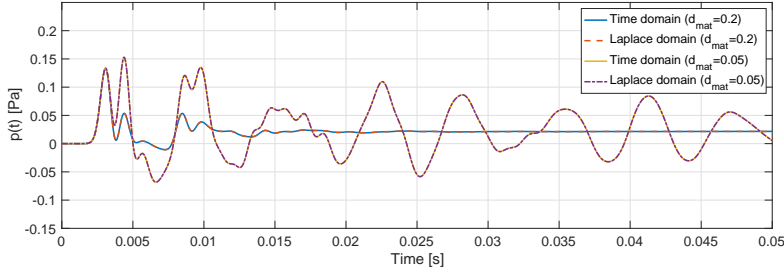
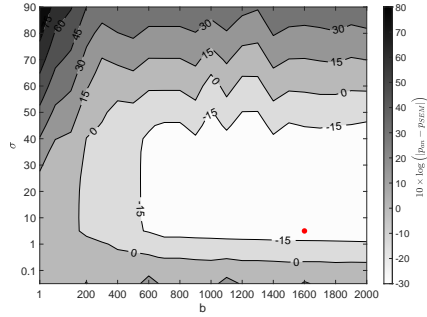
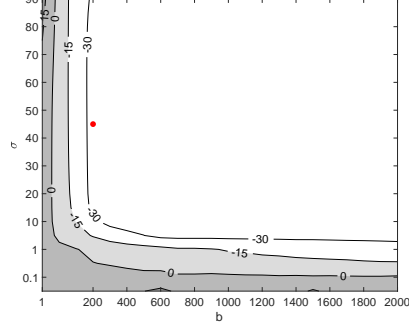


Figure 6: Impulse response simulation with frequency-dependent boundaries for different surface impedance values. The source location is $(s_x, s_y) = (1, 1)$ m and the receiver location is $(r_x, r_y) = (0.2, 0.2)$ m. Simulations were carried out with $P = 4$, $\Delta t = 5.9 \times 10^{-6}$ s, $N_{el} = 15$, $N_s = 3000$ and $(\sigma, b) = (10, 1000)$.

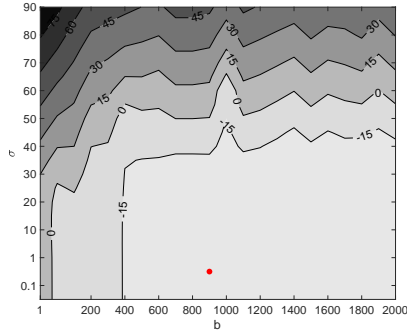
and $Z_s = 2000 \text{ kgs}^{-1}\text{m}^{-2}$. Figure 7 shows the results where the pair of parameter values that provide the lowest error are marked with a red dot. Results show a clear region where the parameters provide a lower error. Thus, the parameters could be chosen for any value that lie inside this region. For the rigid boundary case this region is smaller, whereas it is found to be larger once some absorption occurs at the boundary. As Z_s decreases, i.e., increasing the absorption at the boundaries, the region becomes larger. This finding relieving from an acoustical point of view, as it is very rare to use perfectly rigid boundaries in room acoustics, in most cases some absorption is present at the boundary. Moreover, for $Z_s = 15000 \text{ kgs}^{-1}\text{m}^{-2}$ (Figure 7c) the error is higher than for $Z_s = 2000 \text{ kgs}^{-1}\text{m}^{-2}$ (Figure 7d). This is due to the fact that the impulse response is longer and more complex frequencies N_s are needed to decrease the error. In this analysis the same number N_s is needed to investigate how the parameters change with the different boundary conditions. However, N_s can be chosen to fulfill the accuracy requirements for the more critical case. Note that larger N_s values increase the region where the error is minimized. Figure 7b illustrates this fact when doubling N_s .



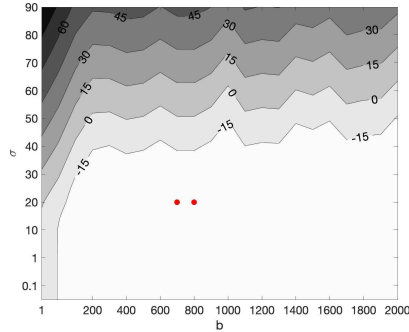
(a) Rigid boundaries with $N_s = 7000$.



(b) Rigid boundaries with $N_s = 14000$.



(c) $Z_s = 15000 \text{ kgs}^{-1} \text{m}^{-2}$ with $N_s = 7000$.



(d) $Z_s = 2000 \text{ kgs}^{-1} \text{m}^{-2}$ with $N_s = 7000$.

Figure 7: Contour plot of the error obtained using 11 equally spaced points for $\sigma \in [0.1, 2000]$ and 11 equally spaced points for $b \in [0.1, 90]$ for three different boundary conditions to obtain (41).

4.3. Reduced Order Model

In this section, model order reduction is applied to different test cases to investigate the benefits of the method. The varying parameter of the system is the absorption properties of the boundaries.

4.3.1. ROM with frequency-independent boundaries

The test case presented in Section 4.2.2 is considered here. The ROM is constructed by generating snapshots when sampling the surface impedance values uniformly $Z_s = [500, 1500, 2500, \dots, 15500] \text{ kgs}^{-1} \text{m}^{-2}$. The reduced basis is then constructed by performing SVD on the snapshot matrix and selecting the

number of singular vectors N_{rb} .

Figure 8 shows the simulation results for different Z_s values that were not present in the snapshot matrix. The number of basis functions ($N_{rb} = 300$) were selected using (47) for an energy value of $E/E_0 = 10^{-6}$. Results show a good match between the ROM and FOM with an absolute error, calculated at the receiver point at $t = 0.1$ s and for $Z_s = 15000 \text{ kgs}^{-1}\text{m}^{-2}$, of $\epsilon = |p_{\text{FOM}} - p_{\text{ROM}}| = 4.3 \times 10^{-9}$ Pa. The relative error for this particular case is given by $\epsilon_{rel} = \left| \frac{p_{\text{FOM}} - p_{\text{ROM}}}{p_{\text{FOM}}} \right| = 6.5 \times 10^{-7}$.

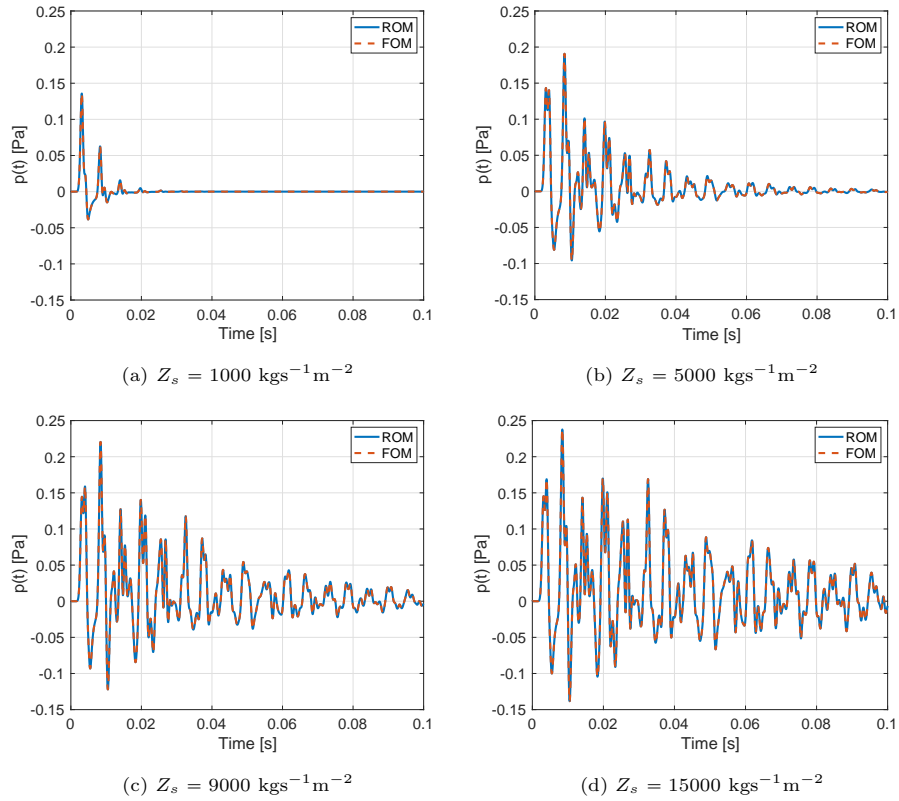


Figure 8: Simulated pressure using the FOM and ROM for different parameter values Z_s with $N_{rb} = 3000$.

The speedup and accuracy of the ROM is investigated by running simulations for different $N_{rb} = [7, 18, 30, 44, 82, 303, 585, 842]$ decay in Figure 9, which also

shows the error and speedups. As expected, decreasing the singular value decay error by including more basis functions to the ROM improves the accuracy but decreases the speedup.

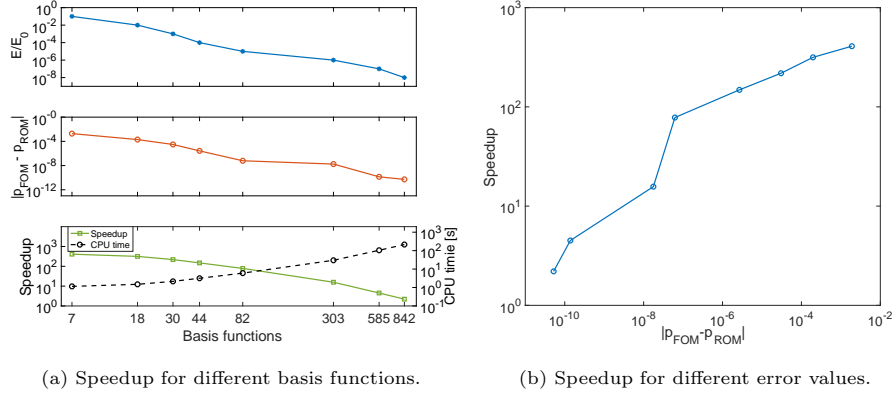


Figure 9: Speedup and error of the ROM with frequency-independent boundaries, for different energy values. Simulations were carried out with a fixed $PPW = 13$ at 1000 Hz, $N_{el} = 20$, $P = 4$, $t = 0.1$ s and $Z_s = 5000 \text{ kgs}^{-1}\text{m}^{-2}$.

The singular value decay and the distribution of the energy among the basis functions is investigated when varying different parameters of the ROM. Figure 10 illustrates the effect on the singular value decay when changing the domain size (a) and (b), the number of complex frequencies N_s (c) and the number of snapshot (d). Figure 10a shows the results when fixing the $PPW = 10$ at 1000 kHz. For a certain energy value, the size of the ROM becomes smaller compared to the FOM when increasing the dimensions of the domain. Table 2 shows an example for $E/E_0 = 10^{-6}$ where the size of the ROM compared to the FOM is given in percentage. This can be explained by the fact that the basis functions needed to capture the dynamics when making the domain larger does increase as rapidly as the increase in DOFs. In Figure 10b, the number of elements per direction is fixed to $N_{el} = 20$. When increasing the size of the domain, the number of basis functions needed increases due to the low resolution. Note that in such cases, the number of PPW decreases when increasing the size of the domain. Figure 10c shows that the basis functions

needed to include certain energy value increases when increasing N_s . Note that the longer the simulation time is, the more complex frequencies are needed. Thus, in practice, longer simulations typically require more basis functions to capture the wave propagation accurately. Finally, the singular value decays are compared for different number of snapshots. Figure 10d shows that the more snapshots are included, the more basis functions are needed which is a result of the sampling technique since the problem is not changed. This illustrates the importance of choosing the minimum number of snapshots that captures the dynamics of the model. Figure 11 presents the error $\epsilon = |p_{\text{FOM}} - p_{\text{ROM}}|$ computed at $t = 0.1$ s in the receiver point $(r_x, r_y) = (0.2, 0.2)$ m to compare the ROM and FOM for different values of Z_s . The ROM was constructed with different number of snapshots to analyze the impact on the accuracy. Increasing the number of snapshots decreases the error. However, the computational time of the offline stage increases with $\mathcal{O}(N_{\text{snapshots}})$.

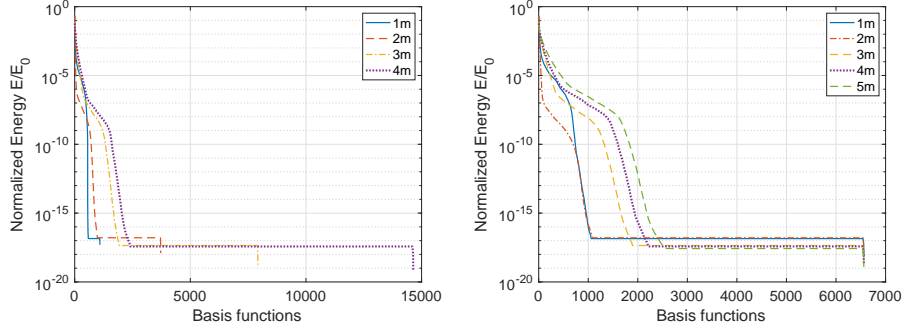
Table 2: Size of the ROM compared with FOM in percentage for $E/E_0 = 1 \times 10^{-6}$.

Domain side length	1 m	2 m	3 m	4 m
ROM vs. FOM size	45.2%	12.3%	11.9%	8.2%

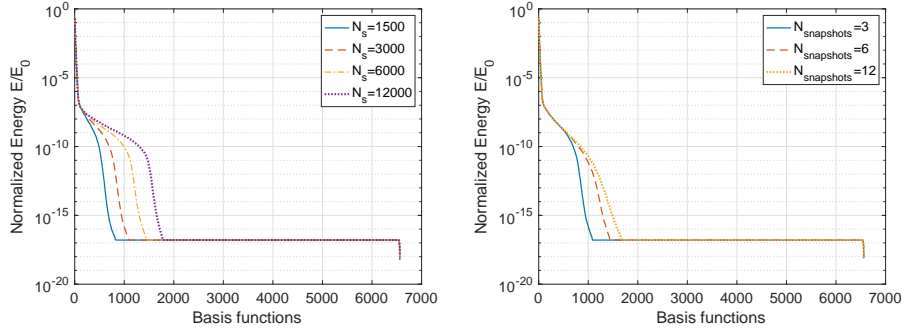
4.3.2. ROM with frequency-dependent boundaries

The test case presented in Section 4.2.3 is now considered again. The thickness of the modeled material is uniformly sampled to generate the snapshots as follows $d_{\text{mat}} = [0.02, 0.07, \dots, 0.22]$ m. The ROM is constructed by applying SVD to the snapshot matrix.

The results, compared with the corresponding FOM high-fidelity solution, are presented in Figure 12. Again, the number of basis functions ($N_{rb} = 150$) were selected to obtain a energy value of $E/E_0 = 10^{-6}$. A good match between the ROM and FOM is presented. The absolute error, calculated at the receiver point at $t = 0.05$ s and for $d_{\text{mat}} = 0.05$ m, is $\epsilon = |p_{\text{FOM}} - p_{\text{ROM}}| = 2 \times 10^{-9}$



(a) Energy decay for different domain side lengths with a fixed $PPW = 10$ at 1000 Hz. (b) Energy decay for different domain lengths with a fixed number of elements $N_{el} = 20$.



(c) Energy decay for different number of complex frequencies N_s . (d) Energy decay for different number of snapshots.

Figure 10: Illustration of computed singular value decay as a measure of the Kolmogorov n -width for different scenarios based on a square domain of size $2 \text{ m} \times 2 \text{ m}$ with frequency-independent BC. $N_{el} = 20$, $t = 0.1 \text{ s}$, $N_s = 3000$ and 3 snapshots.

Pa. Moreover, the relative error for this particular case is $\epsilon_{rel} = \left| \frac{\mathcal{P}_{FOM} - \mathcal{P}_{PROM}}{\mathcal{P}_{FOM}} \right| = 3.6 \times 10^{-7}$.

The speedup for different error values is presented in Figure 13. In this case, the speedup is significantly lower than in the frequency-independent case. The reason is that (58a) is computed in every frequency step, as the boundary contribution changes in each iteration.

Following the same analysis as above, the singular value decay and the distribution of the energy among the basis functions is investigated when varying parameters of the model. Results presented in Figure 14 show similar behaviour

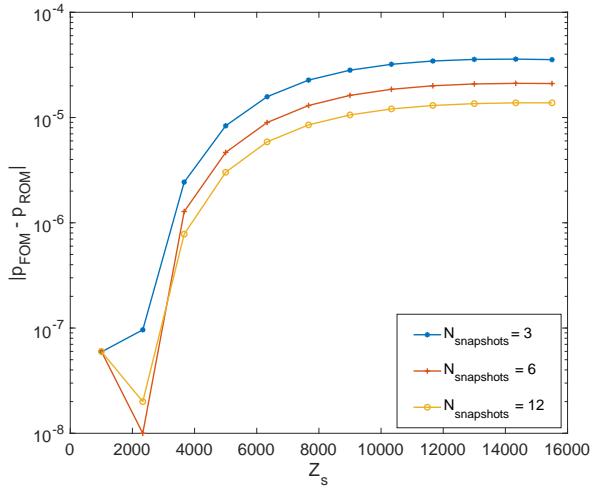


Figure 11: Error between ROM and FOM for different parameter values and number of snapshots using $N_{rb} = 44$ and $E/E_0 = 10^{-4}$.

as described for the frequency-independent case.

5. Discussion

This study demonstrates the benefits of using high-order schemes and RBM techniques for room acoustics. In agreement with previous studies, [4, 8] the use of higher-order schemes accelerates the wave-based room acoustic simulations. We found speedups of five orders of magnitude for an error of 10^{-6} for a polynomial order of $P = 4$. Thus, there is significant improvement in cost-efficiency and accuracy when high-order basis functions are used.

We demonstrate how the ROM can reduce the computational cost significantly when solving the parameterized wave problem. Results agree with previous work from different disciplines, e.g., [63–65], where RBM is used to provide substantial speedups without compromising the accuracy. We demonstrated speedups of more than two orders of magnitude. However, as illustrated in Figures 9 and 13, a compromise between accuracy and speedup occurs. A key challenge is how to choose the proper POD sampling strategy to capture the

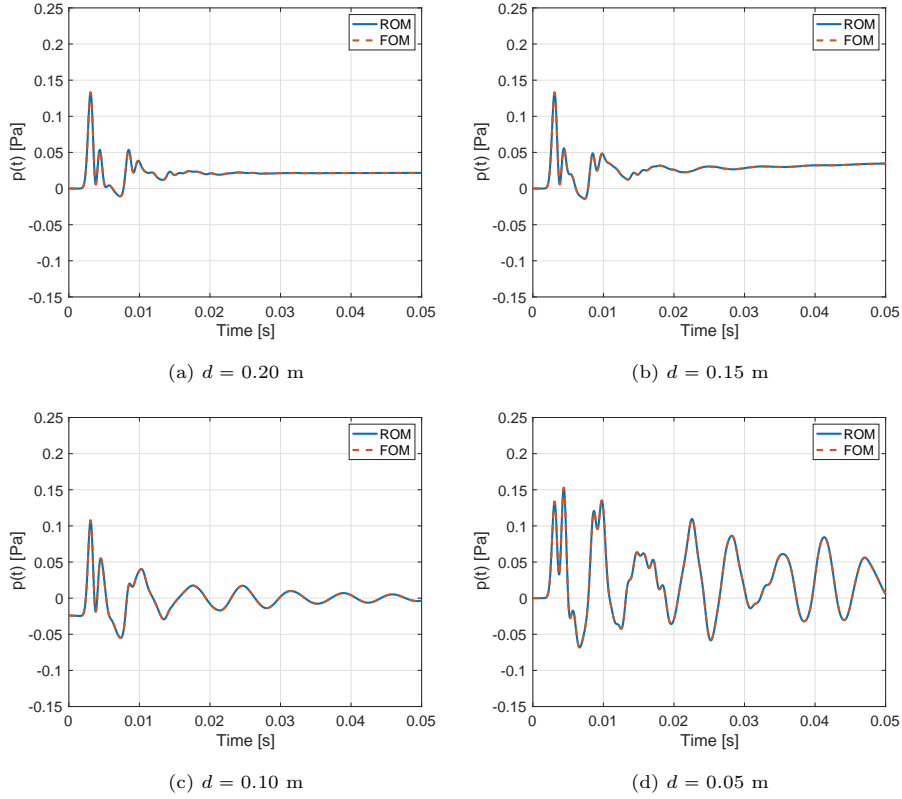


Figure 12: Simulated pressure using the FOM and ROM for different parameter values d_{mat} with $N_{rb} = 3000$.

dynamics of the system with the minimum number of snapshots to minimize the offline stage computational burden. The results show that for a uniform sampling strategy, increasing the number of snapshots produces a slower energy decay of the singular values (Figure 10d), an increased accuracy (Figure 11) and an increase of the offline computational time. In the test case considered, collecting a single snapshot takes 470 s, thus the required time for 3 and 12 snapshots was 1410 s and 5640 s, respectively. In this case, we conclude that the dynamics of the system can be captured accurately with 3 snapshots to cover the whole practical range of interest of the parametrized surface impedance. It is also interesting to highlight that the larger simulation domains are, the

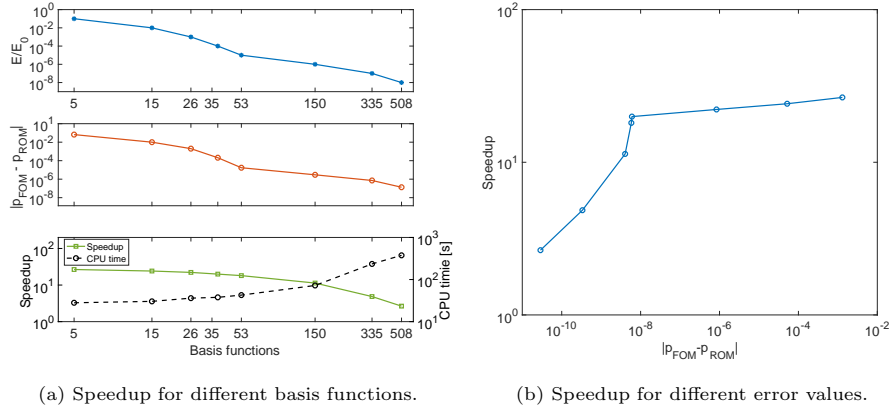
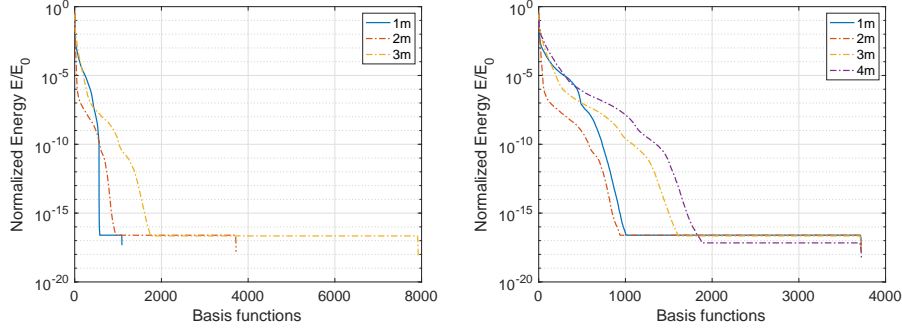


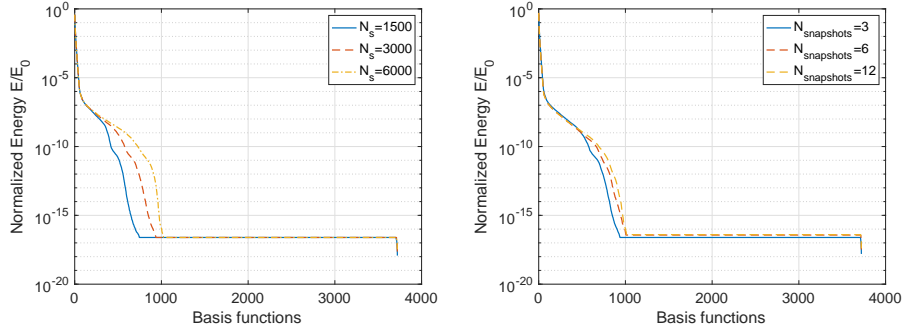
Figure 13: Speedup and error of the ROM with frequency-dependent boundaries, for different energy values. Simulations were carried out with a fixed $PPW = 10$ at 1000 Hz, $P = 4$ and $t = 0.05$ s and $d_{mat} = 0.15$ m.

more favorable to reduce the problem. This indicates that the MOR approach is more beneficial when solving large problems, and in room acoustics problem sizes tend to be very large.

The main drawback of the method is the time signal recovery. On the other hand, the frequency-domain approach circumvents numerical instabilities when reducing the model and it can be more efficient than a time-domain approach if $N_s \ll N_t$. It is also well-suited for parallel computing as the iterations across frequency are all independent of each other. However, the time reconstruction process is not straightforward. The proposed solution for the selection of parameters (41) needs an analytical or time-domain solver solution and is generally expensive to obtain. The parameters sampling resolution used to evaluate (41) plays an important role. High resolution leads to a long computational time. On the other hand, low resolution can miss the optimal parameter values. Furthermore, the free parameters of the Weeks method also depend on the complex frequency numbers N_s , which can be considered as a third parameter that needs to be obtained. The lack of an analytical expression that relates N_s with the maximum frequency and the final simulation time makes the process difficult. If



(a) Energy decay for different domain side lengths with a fixed $PPW = 10$ at 1000 Hz. (b) Energy decay for different domain lengths with a fixed number of elements $N_{el} = 15$.



(c) Energy decay for different number of complex frequencies N_s . (d) Energy decay for different number of snapshots.

Figure 14: Illustration of computed singular value decay for different scenarios based on a square domain of size 2 m with frequency-dependent BC. $N_{el} = 15$, $t = 0.05$ s, $N_s = 3000$ and 3 snapshots.

insufficient number of complex frequencies are chosen, the error increases. A safe choice could be to select N_s as high as possible. This also facilitates the choice of the free parameters σ and b . However, this increases the computational cost of the FOM as more frequencies are evaluated and, moreover, has an impact on the ROM, as more basis functions are needed (Figure 10c). It has been found that the minimized error area of the parameter space decreases when decreasing N_s (Figures 7a and 7b) or when reducing the boundary damping (Figures 7c and 7d). As the free parameters are case dependent, adding absorption to the boundaries allows one to use the same parameter values for a larger number of

different scenarios, compared to a rigid boundary case. Fortunately, in practical room acoustic applications, the boundaries always include damping. From these results, it can be concluded that choosing the proper parameter values is a key point to obtain efficient and accurate results.

The test cases presented in this paper show the potential value of these methods for room acoustics simulations. A typical scenario is to simulate iteratively a room for different absorption properties of the boundaries to find the optimal values that fulfil a specific acoustic requirement. It is shown in Section 4.3 that the ROM allows simulating different parameter values of the boundaries at a significantly lower cost. This implies that the presented framework can be applied to cases where both accuracy and efficiency are needed. This framework can be improved in future work by applying parallel and high-performance computing techniques to overcome the extra computational cost that will be added when moving to a 3D implementation. Moreover, a more efficient strategy for obtaining the parameters for this method is needed.

6. Conclusion

This paper presents a framework to perform room acoustic simulations accurately accounting for all wave phenomena. A high-order discretization scheme based on SEM in the Laplace domain is presented and utilized to build a ROM with parametrized boundary conditions to reduce the computational burden. The framework aims to fulfill the need for accelerating the simulation process in building acoustics when different values of the boundary properties need to be computed for design decisions.

Results confirm that the FOM and ROM schemes have high-order convergence, hence providing accurate and cost-effective room acoustic simulations. The use of RBM results in a decrease in the simulation time by at least one order of magnitude for the frequency-dependent boundaries and two orders of magnitude for the frequency-independent implementation, for the 2D test cases presented here. Results show favourable behaviour in terms of reduction when

increasing the size of the domain, indicating that further accelerations will be possible for problems in 3D.

The drawback of the method is on the choice of the number of complex frequencies and the free parameters selection needed for the time reconstruction by means of Weeks method. The optimal parameter values are case dependent, and the proposed strategy to identify these is computationally expensive. It has been found that the choice of parameters is critical for optimal efficiency and accuracy. However, results show that for a room with materials at the walls that dampens the wave reflections, broader ranges of the Weeks parameters ensure good accuracy, which is relevant for room acoustics as absorption at the boundaries is always included.

Acknowledgments

This work is partly supported by Innovationsfonden, Denmark (Grant ID 9065-00115B), Rambøll Danmark A/S and Saint-Gobain Ecophon A/S, Sweden.

References

- [1] L. Savioja, U. P. Svensson, Overview of geometrical room acoustic modeling techniques, *J. Acoust. Soc. Am.* 138 (2) (2015) 708–730.
- [2] F. Brinkmann, L. Aspöck, D. Ackermann, S. Lepa, M. Vorländer, S. Weinzierl, A round robin on room acoustical simulation and auralization, *J. Acoust. Soc. Am.* 145 (4) (2019) 2746–2760.
- [3] A. Craggs, A finite element method for free vibration of air in ducts and rooms with absorbing walls, *J. Sound Vib* 73 (4) (1994) 568–576.
- [4] F. Pind, A. P. Engsig-Karup, C. H. Jeong, J. S. Hesthaven, M. S. Mejling, J. S. Andersen, Time domain room acoustic simulations using the spectral element method, *J. Acoust. Soc. Am* 145 (6) (2019) 3299–3310.
- [5] D. Botteldooren, Finite-difference time-domain simulation of low-frequency room acoustic problems, *J. Acoust. Soc. Am* 98 (6) (1995) 3302–3308.

- [6] J. A. Hargreaves, L. R. Rendell, Y. W. Lam, A framework for auralization of boundary element method simulations including source and receiver directivity, *J. Acoust. Soc. Am* 145 (4) (2019) 2625–2637.
- [7] H. Wang, I. Sihar, R. P. Munoz, M. Hornikx, Room acoustics modelling in the time-domain with the nodal discontinuous Galerkin method, *J. Acoust. Soc. Am.* 145 (4) (2019) 2650–2663.
- [8] H.-O. Kreiss, J. Oliger, Comparison of accurate methods for the integration of hyperbolic equations, *Tellus* 24 (3) (1972) 199–215.
- [9] J. S. Hesthaven, G. Rozza, B. Stamm, *Certified Reduced Basis Methods for Parametrized Partial Differential Equations*, Springer, 2016.
- [10] A. Quarteroni, G. Rozza, A. Manzoni, Certified reduced basis approximation for parametrized partial differential equations and applications, *J. Math Ind* 1 (3) (2011) .
- [11] N. N. Cuong, K. Veroy, A. T. Patera, Certified real-time solution of parametrized partial differential equations, *Handbook of Materials Modeling*, 2005, pp. 1529-1564.
- [12] G. Rozza, D. B. P. Huynh, A. T. Patera, Reduced basis approximation and a posteriori error estimation for affinely parametrized elliptic coercive partial differential equations, *Archives of Computational Methods in Engineering* 15 (3) (2008) 229–275.
- [13] M. Drohmann, K. Carlberg, The ROMES method for statistical modeling of reduced-order-model error, *SIAM/ASA J. on Uncer. Quant.* 3 (1) (2015) 116–145.
- [14] C. Prud’homme, A. Patera, Reduced-basis output bounds for approximately parametrized elliptic coercive partial differential equations, *Computing and Visualization in Science* 6 (2-3) (2004) 147–162.

- [15] A. Quarteroni, A. Manzoni, F. Negri, *Reduced Basis Methods for Partial Differential Equations: An Introduction*, Springer, 2015.
- [16] G. Berkooz, P. Holmes, J. L. Lumley and, C. W. Rowley, *Turbulence, Coherent Structures, Dynamical Systems and Symmetry*, Cambridge University Press, 1996.
- [17] M. Ohlberger, S. Rave, *Reduced basis methods: Success, limitations and future challenges*, *Proceedings Of The Conference Algoritmy*, 1-12 (2016).
- [18] D. Amsallem, J. Cortial, C. Farhat, *Towards realtime computational-fluid-dynamics-based aeroelastic computations using a database of reduced-order information*, *AIAA J.*, 48 (9) (2010) 2029–2037.
- [19] S. Giere, *Numerical and analytical aspects of pod-based reduced-order modeling in computational fluid dynamics*, PhD thesis, Free University of Berlin, Germany (2016).
- [20] M. Ganesh, J. Hesthaven, B. Stamm, *A reduced basis method for electromagnetic scattering by multiple particles in three dimensions*, *J. Comput. Physics* 231 (23) (2012) 7756–7779.
- [21] Y. Chen, J. S. Hesthaven, *Certified reduced basis methods and output bounds for the harmonic maxwell’s equations*, *SIAM J. Sci. Comput.*, 32 (2) (2010) 970–996.
- [22] M. A. Grepl, *Reduced-basis approximation and a posteriori error estimation for parabolic partial differential equations*, PhD thesis, Massachusetts Institute of Technology, United States (2005).
- [23] R. S. Puri, D. Morrey, A. J. Bell, J. F. Durodola, E. B. Rudnyi, J. G. Korvink, *Reduced order fully coupled structural– acoustic analysis via implicit moment matching*, *Appl. Math. Mod* 33 (11) (2009) 4097–4119.
- [24] U. Hetmaniuk, R. Tezaur, C. Farhat, *Review and assessment of interpolatory model order reduction methods for frequency response structural*

- dynamics and acoustics problems, *Int. J. Num. Meth. Eng.* 90 (13) (2012) 1636–1662.
- [25] J. Herrmann, M. Maess, L. Gaul, Substructuring including interface reduction for the efficient vibro-acoustic simulation of fluid-filled piping systems, *Mech. Sys. Sig. Proc* 24 (1) (2010) 153–163.
- [26] B. M. Afkham, J. S. Hesthaven, Structure preserving model reduction of parametric hamiltonian systems, *SIAM J. Sci. Comput.* 339 (6) (2017) A2616–A2644.
- [27] V. Pereyra, B. Kaelin, Fast wave propagation by model order reduction, *Elec. Trans. Num. Anal* 30 (-) (2008) 406–419.
- [28] V. Pereyra, Wave equation simulation in two-dimensions using a compressed modeler, *Am. J. Comp. Math.*, 3 (-) (2013) 231–241.
- [29] V. Pereyra, Model order reduction with oblique projections for large scale wave propagation, *Am. J. Comp. Math.*, 295 (-) (2016) 103–114.
- [30] C. Bigoni, J. S. Hesthaven, Simulation-based anomaly detection and damage localization: an application to structural health monitoring, *Comput. Meth. Appl. Mech. Eng* 63 (2020) 12896.
- [31] F. Pind, Wave-based virtual acoustics, Ph.D. thesis, Technical University of Denmark, Denmark (2020).
- [32] S. E. Ahmed, S. Pawar, O. San, A. Rasheed, Reduced order modeling of fluid flows: Machine learning, kolmogorov barrier, closure modeling, and partitioning, *AIAA AVIATION 2020 FORUM*-2946.
- [33] B. Moore, Principal component analysis in linear systems: Controllability, observability, and model reduction, *IEEE Trans. Automat. Control* 26 (1) (1981) 17–32.
- [34] D. Amsallem, C. Farhat, Stabilization of projection-based reduced-order models., *Int. J. Num. Meth. Eng.* 91 (4) (2012) 358–377.

- [35] I. Kalashnikova, B. v. B. Waanders, A. S., M. Barone, Stabilization of projection-based reduced order models for linear time-invariant systems via optimizationbased eigenvalue reassignment., invariant systems via optimizationbased eigenvalue reassignment, *Comput. Meth. Appl. Mech. Eng* 272 (2014) 251–270.
- [36] M. W. Hess, G. Rozza, A Spectral Element Reduced Basis Method in Parametric CFD, *Numerical Mathematics and Advanced Applications – ENUMATH 2017*, Springer, in press, ArXiv e-print 1712.06432, 2017.
- [37] M. W. Hess, A. Alla, A. Q. G. Rozza, M. Gunzburger, A spectral element reduced basis method for Navier–Stokes equations with geometric variations, *ICOSAHOM Conference Proceeding*. Submitted. ArXiv preprint 1812.11051 (2018).
- [38] H. Kuttruff, *Room Acoustics*, 5th Edition, Taylor & Francis, 2009, ch. 2.
- [39] Y. Miki, Acoustical properties of porous materials—modifications of delany-bazley models, *J. Acoust. Soc. Jpn.* 11 (1) (1990) 19.24.
- [40] J. F. Allard, N. Atalla, *Propagation of Sound in Porous Media: Modelling sound absorbing materials*, 3rd Edition, Wiley, West Sussex, 2009.
- [41] B. Gustavsen, A. Semlyen, Rational approximation of frequency domain responses by vector fitting, *IEEE Trans. Power Delivery* 14 (3) (1999) 1052–1061.
- [42] A. V. Oppenheim, A. S. Willsky, S. H. Nawab, *Signals and Systems* (2nd Ed.), Prentice-Hall, Inc., USA, 1996.
- [43] ISO, *Acoustics-Measurement of room acoustic parameters-Part 1: Performance spaces*, Standard, International Organization for Standardization - ISO/TC 43/SC 2 Building acoustics (Jun. 2009).
- [44] W. T. Weeks, Numerical inversion of laplace transform using Laguerre functions, *J. Assc. Comp. Mach.* 13 (3) (1966) 419–429.

- [45] H. Dubner, Numerical inversion of laplace transforms by relating them to the finite fourier cosine transform,, *J. Assc. Comp. Mach* 15 (1) (1968) 115–123.
- [46] A. Talbot, The accurate numerical inversion of laplace transforms, *IMA J. Appl. Math* 23 (1) (1979) 97–120.
- [47] D. Duffy, Comparison of three new methods on characteristic problems from applications, *ACM Trans. Math. Softw. (TOMS)* 19 (3) (1993) 333–359.
- [48] J. A. C. Weideman, Algorithms for parameter selection in the Weeks method for inverting the Laplace transform, *SIAM Journal on Scientific Computing* 21 (1999) 111–128.
- [49] R. Piessens, B. Maria, Numerical inversion of the laplace transform using generalised laguerre polynomials, *Proceedings of the Institution of Electrical Engineers*, Vol. 118, IET, pp. 1517-1522 (1971).
- [50] B. Garbow, G. Giunta, J. Lyness, Software for an implementation of Weeks’ method for the inverse laplace transform, *ACM Trans. Math. Softw. (TOMS)* 14 (2) (1988) 163–170.
- [51] C. Clenshaw, A note on the summation of chebyshev series, *Math. Comp.* 9 (51) (1955) 118–120.
- [52] L. Peng, K. Mohseni, Symplectic model reduction of hamiltonian systems, *SIAM J. Sci. Comput.* 38 (1) (2016) A1–A27.
- [53] S. Sherwin, *Dispersion analysis of the continuous and discontinuous Galerkin formulations*, Springer, Berlin, Heidelberg, 2000.
- [54] G. Gassner, D. Kopriva, A comparison of the dispersion and dissipation errors of gauss and gauss-lobatto discontinuous galerkin spectral element methods, *SIAM Sci. Comp.* 33 (5) (2011) 2560–2579.

- [55] G. Seriani, S. P. Oliveira, Optimal blended spectral-element operators for acoustic wave modeling, *Geophysics* 72 (5) (2007) SM95–SM106.
- [56] M. Ainsworth, H. Wajid, Dispersive and dissipative behavior of the spectral element method, *SIAM J. Numer. Anal.* 47 (5) (2009) 3910–3937.
- [57] Y. Geng, G. Qin, J. Zhang, W. He, Z. Bao, Y. Wang, Space-time spectral element method solution for the acoustic wave equation and its dispersion analysis, *Acoust. Sci. Technol.* 38 (6) (2017) 303–313.
- [58] G. Seriani, S. P. Oliveira, DFT modal analysis of spectral element methods for acoustic wave propagation, *J. Comp. Acoust.* 16 (04) (2008) 531–561.
- [59] S. P. Oliveira, On multiple modes of propagation of high-order finite element methods for the acoustic wave equation, in *Spectral and High Order Methods for Partial Differential Equations ICOSAHOM 2016*, edited by M. L. Bittencourt, N. A. Dumont, and J. S. Hesthaven (Springer, Switzerland), 2017.
- [60] F. Q. Hu, M. Y. Hussaini, P. Rasetarinera, An analysis of the discontinuous galerkin method for wave propagation problems, *J. Comp. Phys.* 151 (2) (1999) 921–946.
- [61] J. Saarelma, J. Botts, B. Hamilton, L. Savioja, Audibility of dispersion error in room acoustic finite-difference time-domain simulation as a function of simulation distance, *J. Acoust. Soc Am.* 139 (4) (2016) 1822–1832.
- [62] S. Sakamoto, Phase-error analysis of high-order finite difference time domain scheme and its influence on calculation results of impulse response in closed sound field, *Acoust. Sci. Technol.* 28 (5) (2007) 295–309.
- [63] J. Pomplun, F. Schmidt, Accelerated a posteriori error estimation for the reduced basis method with application to 3d electromagnetic scattering problems, *SIAM/ASA J. on Sci. Comp.* 32 (2) (2010) 498–520.

- [64] G. Pitton, G. Rozza, On the application of Reduced Basis Methods to Bifurcation Problems in Incompressible fluid dynamics, *J. of Sci. Comp.* 73 (2017) 157–177.
- [65] D. P. Huynh, D. J.Knezevic, A. T.Patera, A Laplace transform certified reduced basis method; application to the heat equation and wave equation, *Comptes Rendus Mathematique* 349 (7-8) (2011) 401–405.